Title

Molecular Origins of Near-Infrared Luminescence in Molybdenum and Tungsten Oxyhalide Perovskites

Authors

Morgan, Emily E

Brumberg, Alexandra

Panuganti, Shobhana

et al.

Publication Date

2024-08-15

DOI

10.1021/acs.chemmater.4c00856

Peer reviewed

Molecular Origins of Near-Infrared Luminescence in Molybdenum and Tungsten Oxyhalide Perovskites

Emily E. Morgan,[†] Alexandra Brumberg,[†] Shobhana Panuganti,[‡] Greggory T. Kent,[†] Arava Zohar,[†] Alexander A. Mikhailovsky,[¶] Mercouri G. Kanatzidis,[‡] Richard D. Schaller,[‡,§] Michael L. Chabinyc,[†] Anthony K. Cheetham,[*,†,‖] and Ram Seshadri[*,†,¶]

[†]*Materials Department and Materials Research Laboratory*
University of California, Santa Barbara, California 93106, United States

[‡]*Department of Chemistry*
Northwestern University, Evanston, Illinois 60208, United States

[¶]*Department of Chemistry and Biochemistry*
University of California, Santa Barbara, California 93106, United States

[§]*Center for Nanoscale Materials*
Argonne National Laboratory, Lemont, Illinois 60439, United States

[‖]*Department of Materials Science and Engineering*
National University of Singapore, Singapore 117575, Singapore

E-mail: akc30@cam.ac.uk; seshadri@mrl.ucsb.edu

Abstract

Materials with near-infrared (near-IR) luminescence are desirable for applications in communications and sensing, as well as biomedical diagnostics and imaging. The most used inorganic near-IR emitters rely on precise doping of host crystal structures with select rare-earth or transition metal ions. Recently, another class of materials with intrinsic near-IR emission has been reported. The compositions of these materials were initially described as vacancy-ordered halide double perovskites Cs_2MoCl_6 and Cs_2WCl_6, but further investigation by some of us on the compound reported as Cs_2WCl_6 revealed an oxyhalide instead, with a composition $Cs_2WO_xCl_{6-x}$, where $1 < x < 2$. Here we demonstrate that the Mo compounds similarly possess the composition $Cs_2MoO_xCl_{6-x}$ or $Cs_2MoO_xBr_{6-x}$ where $1 < x < 2$. Preparing the pure halide appears harder for Mo than for W, and we have not succeeded in doing so. The distinctly different composition requires the coordination environment and oxidation state for the Mo and W centers to be reconsidered from what was assumed for the pure halides. In this work, we examine the mechanism for near-IR emission in these materials given their true structures and compositions. We demonstrate that the luminescence is due to the specific d-orbital splitting caused by the presence of oxygen in the distorted $[MOX_5]^{2-}$ octahedra (X is Cl or Br). The fine structure in the emission spectra at low temperatures has been resolved and is attributed to vibronic coupling to the Mo–O and W–O bond stretches. Understanding the true structure and composition of these interesting materials, besides explaining the near-IR luminescence, suggests how this desirable emission can be realized and manipulated.

Introduction

Vacancy-ordered double perovskites, having the general formula A_2MX_6, where A is a monovalent cation, M is a metal in the 4+ oxidation state, and X is a halide anion, are a popular area of study due to their desirable optical properties. One attribute that makes them particularly attractive is that although they exist as extended crystalline solids, their properties can be understood in terms of the molecular orbitals of the $[MX_6]^{2-}$ anion.[1,2] This facilitates a clear understanding of relationships between the composition, structure, and properties in these compounds. Some examples of the ability to manipulate optical properties in this class of materials include doping of Cs_2ZrCl_6[3–5] and Cs_2SnCl_6,[6,7] giving rise to useful properties such as bright white-light emission and near-IR photoluminescence (PL).

Near-IR luminescence is particularly sought-after because of its potential utility in applications ranging from food inspection and biomedical imaging to communication. This is usually achieved by strategic doping of a host crystal structure;[8] therefore, it was somewhat surprising that Cs_2MoCl_6 and Cs_2WCl_6 were reported to exhibit bright and intrinsic near-IR emission. For example, Liu *et al.* found that the room-temperature photoluminescence quantum yield (PLQY) of near-IR emission in Cs_2MoCl_6 was 26%.[9] When these compounds are excited in the visible range, they show broad emission between 900 nm and 1300 nm, and these materials are both easily synthesized and stable under ambient conditions. Additionally, it has been demonstrated that they could be used to make prototype near-IR imaging devices.[9,10] On a similar theme, a recent report has suggested that the compounds $Cs_2Zr_{1-x}Mo_xCl_6$ become near-IR emitters when $x > 0$, *ie.*, Mo^{4+} with its partially filled d manifold, replaces d^0 Zr^{4+}.[11]

Although the initial results presented for Cs_2MoCl_6 and Cs_2WCl_6 were exciting in terms of performance, there are some aspects of the reports that raised questions about the composition of these materials and the mechanism of their luminescence. For example, the reported Raman spectra for these compounds displayed more peaks than would be

expected for crystals with $Fm\bar{3}m$ symmetry. Additionally, the luminescence was reported to occur either through absorption by defect states and several self-trapped excitons with distinct energies[9] or through d-to-d transitions in octahedrally-symmetric Mo^{4+} or W^{4+} ions.[5,10]

Work by some of us on the tungsten compounds has clarified the composition and optical properties of these compounds and has revealed true compositions of $Cs_2WO_xCl_{6-x}$, where $1 < x < 2$.[12] We also found that compounds of the type A_2WCl_6 could only be obtained in an anhydrous and oxygen-free atmosphere, while the compounds A_2MoCl_6 could not be synthesized even under these conditions,[12] potentially reflecting the greater oxophilicity of Mo associated with a stronger second-order Jahn-Teller tendency.[13] Oxyhalide compounds have been reported in older literature,[14,15] but their luminescent properties were not known at that time. Additionally, in previous work focusing on the tungsten-based vacancy-ordered perovskites, we hypothesized that the observed excitation and emission spectra could be explained using a molecular-orbital diagram originally developed for the molybdenyl ion.[16,17] More specifically, the absorption between 400 nm and 500 nm and the emission peaking between 900 nm to 1300 nm appeared to correspond to two distinct d-to-d transitions in these compounds, explaining the large difference in energy between the two. However, at the time, we had not investigated the temperature-dependence of the luminescence or determined the origin of the fine structure observed at low temperatures.

In this work, we start with a complete characterization of the $Cs_2MoO_x(Cl/Br)_{6-x}$ and $Cs_2WO_xCl_{6-x}$ compounds in terms of their single-crystal X-ray structures, compositions, Raman spectroscopy, and magnetic behavior, complementing previous work on tungsten compounds.[12] We then we address the origins of the optical properties. We also show that the behavior observed in the chlorides is present in the bromide compositions, suggesting that other oxyhalide compounds may make good near-IR emitters. Additionally, while the identity of the halide anion can be used to tune the absorption of visible light in

these materials, the emission features are strongly influenced by the character of the $M-O$ bond. This contribution highlights how we can potentially manipulate the absorption and emission energies of other potential oxyhalide-based near-IR emitters.

Experimental Methods

Synthesis of $Cs_2MoO_xCl_{6-x}$ and $Cs_2MoO_xBr_{6-x}$

0.25 mmol of CsCl and 0.125 mmol $MoCl_5$ were combined in 3 mL of concentrated hydrochloric acid (in the case of the oxychloride) or hydrobromic acid (in the case of the oxybromide) in the PTFE liner of a 23 mL Parr hydrothermal vessel. The vessel was heated to 160 °C for 2 days, followed by slow cooling to room temperature. The crystals were separated from the acid and washed with a small amount of ethanol. In the case of the chloride, the crystals were bright green. In the case of the bromide, the crystals were dark red. Crystals were dried in air for 30 minutes at 60 °C and then transferred to a glovebox.

Synthesis of $Cs_2WO_xCl_{6-x}$

0.25 mmol of CsCl and 0.125 mmol WCl_4 were combined in 3 mL of concentrated hydrochloric acid in the PTFE liner of a 23 mL Parr hydrothermal vessel. The vessel was heated to 160 °C for 2 days, followed by slow cooling to room temperature. The green crystals were separated from the hydrochloric acid and washed with a small amount of ethanol. Crystals were dried in air for 30 minutes at 60 °C and then transferred to a glovebox.

Powder X-ray diffraction and Rietveld refinements

Powder X-ray diffraction (PXRD) measurements were performed on a Panalytical Empyrean powder diffractometer in reflection mode with a Cu-Kα radiation source. Struc-

ture and phase-purity were confirmed using the TOPAS software package.[18]

Single crystal X-ray diffraction and refinements

Single-crystal X-ray diffraction data was collected on a KAPPA APEX II diffractometer with an APEX II CCD detector, TRIUMPH monochromator, and Mo-Kα radiation source ($\lambda = 0.71073$ Å). Structure refinements were performed in the SHELXTL software package. Crystal structures were visualized using the VESTA software package.[19]

X-ray photoelectron spectroscopy

X-ray photoelectron spectroscopy measurements were performed using a Thermo Fisher Escalab Xi+ XPS system with a monochromated aluminum anode (1486.7 eV). Powder samples were pressed onto carbon tape and were transferred to the instrument. Since all measured samples were semiconducting, charge compensation was applied and all spectra were referenced to the C $1s$ peak of carbon at 284.5 eV. Data fitting was performed using the CasaXPS software package.

Magnetic measurements and data processing

Magnetic measurements were performed on a Quantum Design MPMS3 Squid instrument, employing DC measurements performed in vibrating sample magnetometry mode. Approximately 10 mg of sample was deposited inside plastic capsules purchased from Quantum Design, which was mounted in a brass sample rod. Magnetization *vs.* temperature measurements were performed at fields of 500 Oe between 1.8 K and 300 K. To calculate the temperature-dependent effective moment for each sample, the magnetization was converted to susceptibility (χ). For the Curie-Weiss fitting, the $1/\chi$ data was fit using Equation 1 between 50 K and 300 K. Here χ_0 is the diamagnetic correction to the susceptibility, T is the temperature, C is the Curie constant, and θ_{CW} is the Weiss temperature.

$$\chi^{-1} = \frac{T - \theta_{CW}}{\chi_0(T - \theta_{CW}) + C} \tag{1}$$

Raman spectroscopy

Raman spectroscopy was performed using a HORIBA Jobin Yvon T64000 open-frame confocal microscope operating at laser wavelengths of 488 nm or 647 nm with a monochromator and LN_2-cooled CCD array detector. Calibration was confirmed by referencing the spectrum of monocrystalline silicon, which has a peak at 521 cm^{-1}. For variable-temperature measurements, samples were pressed onto copper tape and sealed inside a vacuum chamber, where temperature was controlled using a nitrogen flow with a Lake Shore Cryotronics temperature controller. The sample was allowed to equilibrate at each temperature point for 15 minutes prior to data collection.

UV-vis spectroscopy

Absorbance spectra were obtained by measuring diffuse reflectance on a Shimadzu UV3600 UV-Vis-NIR spectrometer equipped with an integrating sphere. Samples were diluted in barium sulfate. Reflectance was converted to absorbance using the Kubelka-Munk transformation.[20]

Near-IR fluorimetry

Samples were encapsulated in poly(methyl methacrylate) (PMMA) and mounted on a glass slide. A PTI Quantamaster fluorimeter equipped with a near-IR detection system and a 950 nm long-pass filter was used for all measurements. For the excitation scan, the emission at 1000 nm was monitored while scanning the excitation wavelength between 350 nm and 800 nm. The final spectra were obtained by normalizing the raw data by the intensity of the lamp for this spectral range.

Photoluminescence measurements

For the experiments conducted using 400 nm excitation, temperature-dependent continuous-wave (CW) and time-resolved PL experiments were performed using the 400 nm frequency-doubled output of a Ti:sapphire amplifier with 2 kHz repetition rate and 35 fs pulse width. Temperature-dependent PL spectra of powder samples were collected via front-face excitation in a helium closed-cycle cold-finger cryostat. Samples were equilibrated for 5 minutes at each temperature point prior to data collection. Spectra were collected using a 100 μW near-IR detector with a range of 800 nm to 1300 nm. Time-resolved PL data were collected with time-correlated single photon counting electronics using a CCD detector. For the experiments conducted using a 800 nm excitation, powder samples were encapsulated in RTV silicone (Momentive RTV615) on a quartz coverslip and then mounted in a liquid nitrogen cryostat connected to a temperature controller. Near-IR emission spectra were collected on two different detectors to capture the full emission region. To obtain emission in the range of 850 nm to 1050 nm, the samples were photoexcited using the 800 nm pulsed laser light generated by a Ti:Sapphire regenerative amplifier (Coherent Astrella) with the repetition rate of 5 kHz. The resulting emission was collected in a 90 degree geometry after passing through a long pass filter into the entrance slit of a spectrometer connected to a CCD detector (Princeton Instruments PIXIS-400). The same setup was used to collect the time-resolved PL data. In these measurements, the light was detected by a Si avalanche photodiode (Micro Photon Devices PDM) mounted on the secondary port of the spectrometer. Photon counts were analyzed by a multiscaler/analyzer (Becker and Hickl MSA-300) to obtain the PL decay traces. To obtain emission in the range of 900 nm to 1400 nm, samples were photoexcited using an 808 nm continuous wave laser diode (Coherent OBIS) and modified NIR fluorimeter (PTI Quantamaster) with liquid nitrogen-cooled Ge detector. The PL emission was passed through an 850 nm long-pass edge filter and focused onto the input slit of the fluorimeter. The data were acquired using PTI's Felix 32 software. The spectra acquired from these two

methods were then stitched together to obtain a complete near-IR emission spectrum for the range 850 nm to 1700 nm. For analysis of the CW spectra, the abscissa was converted to units of eV using the standard relation $E = hc/\lambda$. In order to account for the difference between wavelength- and energy-dependent spectra, the ordinate was transformed using Equation 2. Gaussian peak-fitting of the CW spectra and exponential decay fitting of the time-resolved spectra was performed using the Fityk software package.[21]

$$I_E = I_\lambda \lambda^2 (hc)^{-1} \tag{2}$$

Results and Discussion

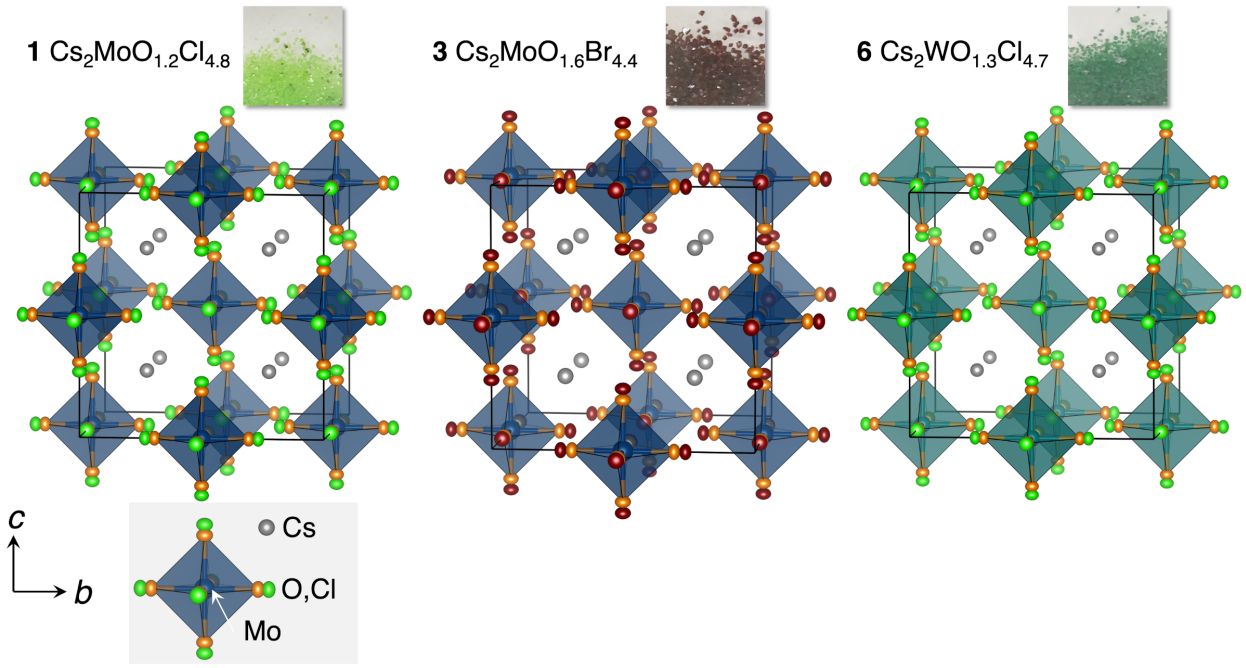

Figure 1: Single-crystal X-ray structures of three representative samples of the oxyhalides: **1** $Cs_2MoO_{1.2}Cl_{4.8}$, **3** $Cs_2MoO_{1.6}Br_{4.4}$ and **6** $Cs_2WO_{1.3}Cl_{4.7}$ refined using a split-site model with halide and oxygen on the ligand sites. All structures are drawn to scale and thermal ellipsoids are depicted at 50 % probability. Photographs of the three samples are presented alongside.

The single-crystal X-ray structures of three different crystals are shown in Figure 1.

Table 1: Details of the six different single crystal structures of oxyhalides determined in this study.

Sample	Composition	*M*:*X* from XPS	Cell a (Å)	*M*–*X* (Å)	*M*–O (Å)	R
1	$Cs_2MoO_{1.2(1)}Cl_{4.8(1)}$	1:5.0	10.216(5)	2.367(4)	1.97(6)	2.2 %
2	$Cs_2MoO_{1.5(2)}Cl_{4.5(2)}$		10.197(5)	2.360(4)	2.02(5)	3.1 %
3	$Cs_2MoO_{1.60(5)}Br_{4.40(5)}$	1:4.3	10.613(7)	2.516(3)	2.06(4)	3.1 %
4	$Cs_2MoO_{1.74(5)}Br_{4.26(5)}$		10.624(6)	2.520(2)	2.10(4)	3.3 %
5	$Cs_2WO_{1.1(1)}Cl_{4.9(1)}$	1:5.4	10.23(2)	2.370(6)	1.90(7)	3.0 %
6	$Cs_2WO_{1.3(1)}Cl_{4.7(1)}$		10.208(3)	2.369(5)	2.01(7)	2.4 %

All compounds crystallize in the space group $Fm\bar{3}m$. The sample labels and the refined compositions for six crystals (from distinct synthetic batches) are presented in Table 1. It is possible to refine the crystal structures of these compounds with incorrect compositions of Cs_2MoCl_6, Cs_2MoBr_6, and Cs_2WCl_6 and obtain relatively low R-factors. However, as discussed in our prior contribution of the Cs–W–Cl system,[12] the ligand site, which is a single site in the $Fm\bar{3}m$ space group, can be split between O and *X* (where *X* is Cl or Br). Refinement of their positions and occupancies (constraining the occupancy of O + *X* to add up to unity) results in a significant decrease in the R-factors, pointing to better refinements. The high degree of accuracy with which single-crystal X-ray diffraction is able to resolve the O:*X* ratio and their distinct positions is associated with the high symmetry, the simplicity of the structure, and the high quality of the data. Furthermore, the refinements are stable with reliable anisotropic thermal displacement parameters being refined. For example, in **1** $Cs_2MoO_{1.2}Cl_{4.8}$, the R-factor without oxygen is 3.14%, while with oxygen it is 2.20%. From the duplicate syntheses and crystal structure refinements presented in Table 1, it is evident that precise control of O:*X* ratios is somewhat difficult even under identical synthesis conditions.

It is also evident that for every pair of compounds from the same compositional family, larger O:*X* ratios (which mean an oxidation state for Mo or W that is closer to 6+) result in smaller cell parameters and smaller *M*–*X* distances. Interestingly, within the uncertainly of the structure refinement, *M*–*O* distances remain nearly the same across samples. Crys-

tallographic information files from the six crystal refinements are presented as Supporting Information. As stated previously, the refined oxygen content can vary sample-to-sample, even when the same synthesis conditions are used. For the chlorides, the refined oxygen coefficient tends to be between 1.0 and 1.5. For the bromide, there is usually a larger amount of oxygen, with x generally between 1.5 and 2. We have also attempted to synthesize the tungsten-based oxybromide, but the crystals were of poor quality, making the composition difficult to determine. For this reason, this sample was excluded from this study. Phase purity and unit cell parameter trends were also validated using powder X-ray diffraction. Additional details of the powder diffraction data are presented in the Supporting Information.

X-ray photoelectron spectroscopic studies were carried out on samples **1** $Cs_2MoO_{1.2(1)}Cl_{4.8(1)}$, **3** $Cs_2MoO_{1.60(5)}Br_{4.40(5)}$, and **5** $Cs_2WO_{1.1(1)}Cl_{4.9(1)}$. High resolution XPS scans of the W 4f and Mo 3d regions in compounds are presented in the Supporting Information. Analysis of the XPS data support the compositions above. The pure halides would be expected to display the 4+ oxidation state, whereas the oxychlorides and oxybromides studied here would be expected to possess oxidation states closely to 5+, from the measured compositions. **1** $Cs_2MoO_{1.2}Cl_{4.8}$, the Mo 3d-5/2 peak is found at an energy of 232.3 eV, which is consistent with an oxidation state closer to 5+ than 4+, indicative of the presence of the oxychloride.[22] A more precise analysis of the oxidation state from XPS proved challenging because of the absence of standards for these elements in these oxidation states, and because spectral interference in the relevant regions from the orbital states of other atoms obscures fitting. Similarly, it was difficult to obtain quantitative estimates for the relative amount of O in the compounds potentially due to adventitious adsorbed oxygen; this is a well-known problem in XPS. However, *M*:*X* ratios from XPS do appear to follow the trends from the more accurate crystallography, and while not reproducing precise values, serve to strengthen suggestions that the *M*:*X* is never the expected 1:6 for a pure halide. These values are also presented in Table 1.

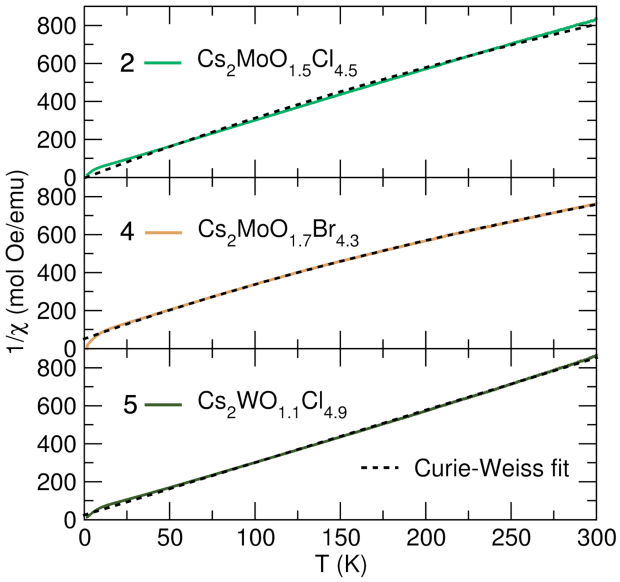

Figure 2: Curie-Weiss fits carried out between $T = 30\,\mathrm{K}$ and $300\,\mathrm{K}$ along with the measured temperature-dependent susceptibility of **2** $Cs_2MoO_{1.5}Cl_{4.5}$, **4** $Cs_2MoO_{1.7}Br_{4.3}$, and **4** $Cs_2WO_{1.1}Cl_{4.9}$.

Table 2: Curie Weiss fitting parameters for the three samples on which magnetic measurements were carried out displaying consistent values with the O:*X* ratios suggested by single-crystal X-ray refinements.

Composition	**2** $Cs_2MoO_{1.5}Cl_{4.5}$	**4** $Cs_2MoO_{1.7}Br_{4.3}$	**5** $Cs_2WO_{1.1}Cl_{4.9}$
Weiss temperature (K)	1.04	−15.74	−8.92
Curie constant (μ_B^2)	0.290	0.301	0.362
Effective moment (μ_B)	1.52	1.55	1.70

In addition to crystallography, magnetic measurements were performed in order to provide further evidence for the sample compositions established by single-crystal X-ray analysis. High-temperature (meaning at temperatures that correspond to the paramagnetic regime of magnetism) magnetic susceptibility is a useful and accurate measurement technique to establish the number of unpaired electrons and therefore the oxidation state in pure samples of materials.[23] These measurements were performed on samples **2**, **4**, and **5**. The general observations and conclusions for these measurements remain valid for the other samples, regardless of slight variations in stoichiometry. Plots of the magnetic data and corresponding Curie Weiss fits are shown in Figure 2, with all fitting parameters shown in Table 2. Very little evidence for long-range magnetic ordering is seen in any of the samples as a consequence of the large physical distance separating magnetic centers in this structure type, and the absence of charge carriers.

As discussed in some of our previous work,[12] since the paramagnetic species in these compounds are $[MOX_5]^{2-}$ ions, the magnetic behavior is consistent with that of a spin-only d^1 compound. This is because the magnetic Mo and W are in a 5+ oxidation state (with some in the non-magnetic 6+ state for charge compensation) and because the $M-O$ bond breaks the octahedral symmetry, thereby quenching orbital angular momentum. In contrast, we have previously shown that the pure W^{4+} halide Cs_2WCl_6 with its d^2 configuration does not follow Curie-Weiss behavior as a consequence of unquenched orbital angular momentum.[12] In the case of the Mo-based compounds, the measured effective moments of 1.52 μ_B and 1.55 μ_B are slighly less than the expected moment for a spin-only d^1 ion which is 1.73 μ_B. This observation can be rationalized by the fact that these compounds contain extra oxygen (beyond O:*X* of 1:5) and therefore a larger number of $[MoO_2X_4]^{2-}$ octahedra containing Mo^{6+} ions, which are d^0 and non-magnetic. In the case of sample **5** $Cs_2WO_{1.1}Cl_{4.9}$ the compound primarily contains W^{5+} ions, and therefore its measured moment is very close to the expected value. Magnetic measurements therefore provide an accurate confirmation of the d-electron count which in turn, supports the compositions

assigned by single-crystal X-ray diffraction.

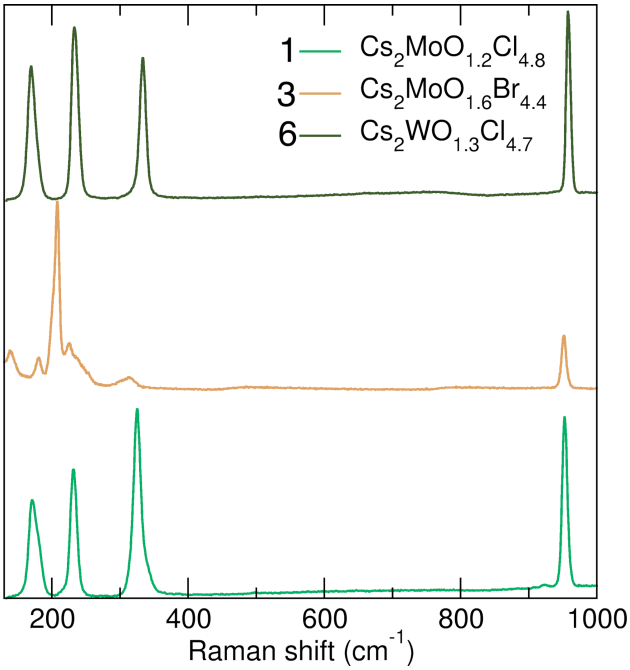

Figure 3: Room temperature Raman spectra of **1** $Cs_2MoO_{1.2}Cl_{4.8}$, **3** $Cs_2MoO_{1.6}Br_{4.4}$, and **6** $Cs_2WO_{1.3}Cl_{4.7}$.

Room temperature Raman spectra of samples **1**, **3**, and **6** are displayed in Figure 3. In the case of the chlorides an excitation wavelength of 488 nm was used, while for the bromide a wavelength of 647 nm was used. These wavelengths were chosen to minimize overlap with the optical absorption maxima of the samples (described in further detail below), which prevents resonance effects in the spectra. First, considering the spectra for **1** $Cs_2MoO_{1.2}Cl_{4.8}$ and **5** $Cs_2WO_{1.3}Cl_{4.7}$, we find that they are qualitatively quite similar due to similarities in composition and metal-ligand bond lengths. In these compounds, the majority of the octahedra are expected to have a composition of $[MOCl_5]^{2-}$, which has a point group symmetry of C_{4v}. In this case, group theory predicts that there can be up to 11 Raman-active modes observed, in contrast to the 3 modes expected for the O_h symmetry of the pure halide. In the low-frequency region for **2** $Cs_2MoO_{1.2}Cl_{4.8}$ peaks are located at 173.4 cm^{-1}, 231.9 cm^{-1}, and 325.0 cm^{-1}, while in $Cs_2WO_{1.3}Cl_{4.7}$ there are peaks at 170.5 cm^{-1}, 233.8, cm^{-1} and 333.6 cm^{-1}. Based on their similarity to the modes present in

other vacancy-ordered systems, these features can be assigned to the bending, asymmetric stretching, and symmetric stretching modes of the $M-$Cl bonds. In other cases where local octahedral symmetry is broken, such as in *X*-site alloying in the Cs_2TeX_6 compounds (which are not prone to form oxyhalide species), the additional peaks which correspond to this lowering in symmetry are found between 100 cm^{-1} and 300 cm^{-1}.[24] However, in the case of the compounds studied here, an additional peak appears at significantly higher energies due to the difference in the strength of the *M*–O bonds compared to *M*–*X* bonds. These higher energy peaks are observed at 958.2 cm^{-1} in **5** $Cs_2WO_{1.3}Cl_{4.7}$ and 953.0 cm^{-1} in **2** $Cs_2MoO_{1.2}Cl_{4.8}$ and correspond to the *M*–O bond stretches.

In contrast to the all-chloride compositions, the peaks for $Cs_2MoO_{1.6}Br_{4.4}$ show additional peaks which do not appear in the chloride compositions. This difference can be attributed to the fact that this composition contains more oxygen compared to the chlorides. In $Cs_2MoO_{1.6}Br_{4.4}$ we expect that, in addition to octahedra with the composition $[MoOBr_5]^{2-}$, there will also be more octahedra with of the type $[MoO_2Br_4]^{2-}$ compared to the chloride compositions. Although there is no crystal structure reported for the compound $Cs_2MoO_2Br_4$, literature on related compounds suggests that the two oxygens in the octahedra will be arranged in a *cis* configuration.[25] Therefore, the expected point group for these octahedra is C_{2v}, which can contribute up to 15 additional Raman-active modes, thus explaining why several additional peaks are visible. As in the case of the chlorides, the peaks at lower energies should correspond to motions of the Mo – Br bonds, while the peak at 951.7 cm^{-1} represents the Mo – O bond stretch. In summary, the compositions from single crystal diffraction and the Raman spectra are consistent with one another, where in $Cs_2MoO_{1.2}Cl_{4.8}$ and $Cs_2WO_{1.3}Cl_{4.7}$, the most common species are the $[MOCl_5]^{2-}$ octahedra, while in $Cs_2MoO_{1.6}Br_{4.4}$ there appears to be a significant amount of both $[MoOBr_5]^{2-}$ and $[MoO_2Br_4]^{2-}$ octahedra. We do not expect to observe a significant number of $[MX_6]^{2-}$ octahedra in any of the compounds as these are expected to be unstable in the presence of air.[12]

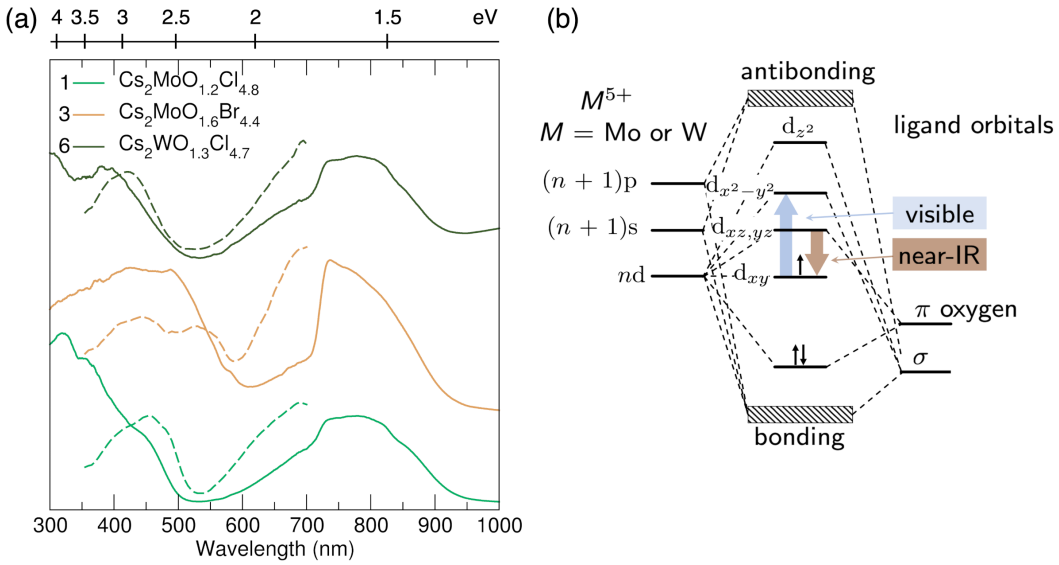

Figure 4: (a) Normalized UV-vis absorption spectra (solid traces) and near-IR fluorimetry excitation scans for emission detected at 1000 nm (dashed traces) for **1** $Cs_2MoO_{1.2}Cl_{4.8}$, **3** $Cs_2MoO_{1.6}Br_{4.4}$, and **6** $Cs_2WO_{1.3}Cl_{4.7}$. Note that all spectra have been shifted and re-scaled along the vertical axis for visual comparison. (b) Re-drawn molecular-orbital diagram developed by Gray and co-workers[16] for d^1 metal oxyhalides.

The absorption spectra for all compounds are shown as the solid lines in Figure 4(a). In order to clarify the origin of absorption features in these compounds, we have reproduced aspects of a molecular-orbital diagram developed by Gray and co-workers for the $[MOX_5]^{2-}$ ions[16,17] in Figure 4(b). First, we consider the lower energy transition, where the absorption onset appears at approximately 930 nm in the molybdenum-based compositions and approximately 920 nm in the tungsten-based compound. This absorption was previously reported to arise from the presence of defect states;[9] however, considering past work on the spectroscopy of the $[MOX_5]^{2-}$ ions, it is clear that this feature is actually due to a transition from the d_{xy} orbital to the $d_{xz,yz}$ orbitals. The energy of this transition is primarily influenced by the interaction of the metal center and the oxygen π orbitals, which explains why the absorption onset is slightly different for the tungsten- and molybdenum-based compositions. Next, we consider the higher-energy absorption feature, where the absorption onset for the chlorides occurs at approximately 510 nm, while the onset for the bromide occurs at 620 nm. The energies of these absorption features also correspond to

the visual appearances of these compounds, where both chlorides are green, while the bromide is a dark red. This feature is attributed to the transition between the d_{xy} and $d_{x^2-y^2}$ orbitals. In this case, the transition energy is most influenced by the interaction between the metal and halide ligands. Therefore, the bromide, which has weaker metal-halide bonding than the chlorides, absorbs at lower energies. For all of the compounds, below 400 nm the absorption spectrum features additional peaks that arise from higher energy d-to-d and ligand-to-metal charge transfer transitions.

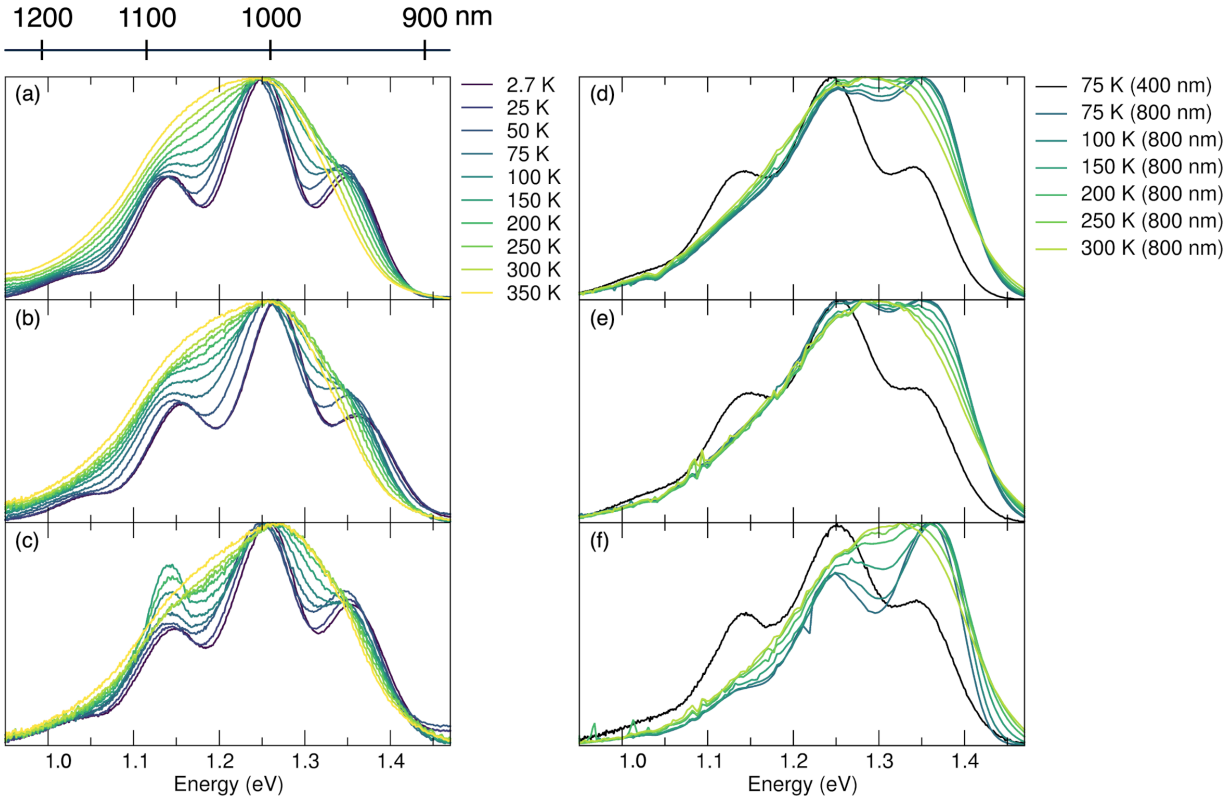

Figure 5: Normalized variable-temperature near-IR emission spectra under 400 nm excitation for (a) **1** $Cs_2MoO_{1.2}Cl_{4.8}$, (b) **3** $Cs_2MoO_{1.6}Br_{4.4}$, and (c) **6** $Cs_2WO_{1.3}Cl_{4.7}$. Normalized variable-temperature near-IR emission spectra under 800 nm excitation (with a 400 nm spectrum for visual comparison) for (d) **1** $Cs_2MoO_{1.2}Cl_{4.8}$, (e) **3** $Cs_2MoO_{1.6}Br_{4.4}$, and (f) **6** $Cs_2WO_{1.3}Cl_{4.7}$. All data plotted in energy (eV) rather than wavelength to clearly demonstrate the energy splitting of the peaks.

After establishing the absorption properties of the tungsten and molybdenum oxyhalides, we sought to investigate the origin of the near-IR emission in these materials. The first question to be addressed is which transitions in these materials give rise to the

reported near-IR emission, which is also shown in Figure 5. As illustrated by the UV-vis spectra and molecular orbital diagram, there are several possible scenarios which could produce near-IR emission. The first is that for excitation wavelengths in the range of 400 nm to 500 nm, an electron could be promoted from d_{xy} to $d_{x^2-y^2}$ and radiatively decay to the $d_{xz,yz}$ states, followed by decay back to d_{xy}. The work of Gray and co-workers suggests that the difference in energy between the $d_{x^2-y^2}$ and $d_{xz,yz}$ states is approximately 1.14 eV (1087 nm), which is similar to the energy of the emission. A second possibility is that the emission arises from radiative decay from the $d_{xz,yz}$ states to the d_{xy} ground state. Based on the absorption onsets in the UV-vis spectra, the energy of this transition is between 1.34 eV and 1.50 eV (925 nm and 827 nm). In this case, the Stokes shift between the absorption and the emission would be between approximately 200 meV and 300 meV. In order to determine which of these transitions is responsible for the emission, near-IR fluorimetry excitation scans were used, shown in dashed lines in Figure 4. Here, the intensity of the emission at 1000 nm was monitored while scanning the excitation wavelength. The results of the fluorimetry experiments suggest that exciting either of the first two d-to-d transitions can produce near-IR emission; however, the fact that the emission is still observed and is more intense for lower energy (longer wavelength) excitation suggests that the emission comes from the $d_{xz,yz}$ to d_{xy} transition. In the case of the higher-energy excitation, we hypothesize that the emission comes from initially promoting an electron to the $d_{x^2-y^2}$ state, followed by non-radiative decay to $d_{xz,yz}$, and then followed by radiative decay to the d_{xy} state.

To further confirm which d-to-d transitions produce near-IR emission in these compounds and to establish why multiple peaks are visible in the emission spectra, variable-temperature photoluminescence (PL) spectra were obtained using excitation wavelengths of 400 nm and 800 nm. Steady state emission spectra are shown in Figure 5, while the results of time-resolved experiments are summarized in Figure 6. The spectra for all three samples are very similar in shape and energy range, with the largest differences occurring

between the Mo-containing and W-containing samples. This observation can be rationalized by the fluorimetry data and the MO diagram. Assuming that the near-IR emission is a transition between the $d_{xz,yz}$ and d_{xy} states, as indicated by the fluorimetry data, then the energy of the transition should be most sensitive to the strength of the metal-oxygen bond. Therefore, it makes sense that the Mo- and W-containing compounds have similar, but not identical emission spectra. The general similarities between the 400 nm and 800 nm spectra again suggest that the emission occurs from a $d_{xz,yz}$ to d_{xy} transition, as the 800 nm excitation only has sufficient energy to access the $d_{xz,yz}$ states.

Next, we address why multiple peaks are present in the emission, which are most apparent at low temperatures. In a previous report, the multiple emission features were attributed to the presence of several self-trapped excitons associated with different structural distortions.[9] Others have suggested that the emission arises from d-to-d transitions in Mo^{4+} or W^{4+} in an octahedral crystal field accompanied by vibronic coupling.[5,10] However, these explanations do not account for the fact that the emitting species in these compounds have the formula $[MOX_5]^{2-}$ rather than $[MX_6]^{2-}$ Therefore, here we consider a hypothesis which takes into account both the correct composition of these materials and the consistent peak splitting pattern observed in the emission. Specifically, we find that the energy of the splitting in the emission is similar to the energy of the $M-$O stretches observed in the Raman spectra of these compounds. For example, in $Cs_2WO_{1.3}Cl_{4.7}$ at 100 K we find that the splittings between the three most prominent peaks in the 400 nm emission spectra are 0.113 eV and 0.101 eV (average splitting of 0.107 eV). In the 800 nm spectra at 100 K, the splittings are 0.111 eV and 0.122 eV (average of 0.117 eV). For comparison, the energy of the W – O stretch at that temperature is 958.8 cm^{-1} (0.119 eV) in $Cs_2WO_{1.3}Cl_{4.7}$ (as shown in Figure 7). This suggests that the fine structure of the emission in these compounds arises from vibronic coupling to the $M-$O stretches.

Under 800 nm excitation, the emission of the different samples broaden as the temperature is raised as a consequence of the usual physics of phonons as described using

the Huang-Rhys theory.[26] The blue-shifted feature that grows with with increasing temperature seen in the 800 nm excited samples can be the result of a few different physical processes. In conventional semiconductors, such blue shifts are sometimes attributed to charge carriers, which is not believed to be the case here. Previously, the blue-shift of photoluminescence in related halide perovskite materials have been attributed to significant thermal expansion effects[27,28] which could be playing a role here. The question of why this blue-shifted feature is more noticeable with 800 nm excitation and not with the 400 nm excitation is not entirely clear at this time.

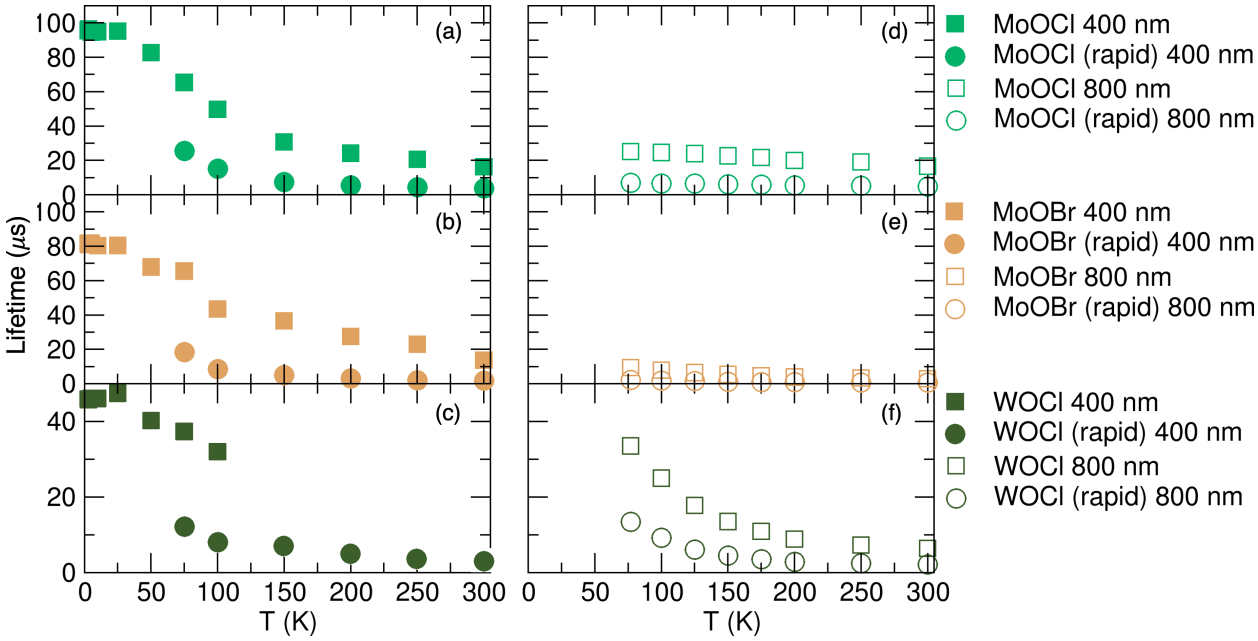

Figure 6: Temperature dependence of the emission lifetimes under 400 nm excitation for (a) **1** $Cs_2MoO_{1.2}Cl_{4.8}$, (b) **3** $Cs_2MoO_{1.6}Br_{4.4}$, and (c) **6** $Cs_2WO_{1.3}Cl_{4.7}$. Temperature dependence of the emission lifetimes under 800 nm excitation for (d) **1** $Cs_2MoO_{1.2}Cl_{4.8}$, (e) **3** $Cs_2MoO_{1.6}Br_{4.4}$, and (f)**6** $Cs_2WO_{1.3}Cl_{4.7}$. Square and circle symbols indicate the two lifetimes that resulted from bi-exponential fitting.

Finally, in order to provide a more complete picture of the luminescence in these compounds, we have investigated the temperature dependence of the emission lifetimes, shown in Figure 6. As in the steady state experiments, all data were collected using 400 nm and 800 nm excitation. In all compounds, the lifetime was measured by measuring the emission at the wavelength corresponding to the most intense emission.

With 400 nm excitation, we find that at low temperatures, all compositions show long emission lifetimes of approximately 95 μs for $Cs_2MoO_{1.2}Cl_{4.8}$, 80 μs for $Cs_2MoO_{1.6}Br_{4.4}$, and 45 μs for $Cs_2WO_{1.3}Cl_{4.7}$. These long lifetimes persist for temperatures between 2.7 K and 25 K. In the temperature range between 50 K and 150 K, all compounds show a sharp decline in the emission lifetime. In the Mo-based compounds for temperatures greater than 75 K, the behavior of the emission decay becomes more complex, requiring two exponential functions to fit the emission profiles. In $Cs_2WO_{1.3}Cl_{4.7}$, at 75 K and 100 K the emission is best fit by a bi-exponential, but at 150 K, it is again possible to model the emission decay with a single exponential. Therefore, in this compound it is possible that there are either two processes with similar lifetimes, or there is a complete transition from the longer-lifetime process occurring at low temperatures to the shorter-lifetime process at high temperatures.

For the 800 nm excitation, the lifetimes were measured in a temperature range of 77 K to 300 K. All compounds show overall shorter lifetimes for the 800 nm excitation in comparison to the 400 nm excitation, where the difference is especially apparent at lower temperatures. Again, both Mo-based compounds show very similar trends in lifetime with temperature, with $Cs_2MoO_{1.2}Cl_{4.8}$ having slightly longer lifetimes compared to $Cs_2MoO_{1.6}Br_{4.4}$. The behavior of $Cs_2WO_{1.3}Cl_{4.7}$ also differs somewhat from that of the Mo-based compounds and appears more similar to the 400 nm data collected on this same compound. Again at 77 K there are two lifetime components with clearly different lengths (33 μs and 13 μs) which are similar to those observed in the 400 nm data. These components also show a temperature dependence similar to that of the 400 nm data set.

We have also examined the variable-temperature Raman spectra between 80 K and 300 K for $Cs_2WO_{1.3}Cl_{4.7}$, as shown in Figure 7, in order to check for phase transitions or other changes in the vibrational spectrum that could be connected to the temperature-dependent optical properties. The Raman spectra in (a) and (b) show only small changes, indicating that the crystal structure does not undergo a phase transition within this tem-

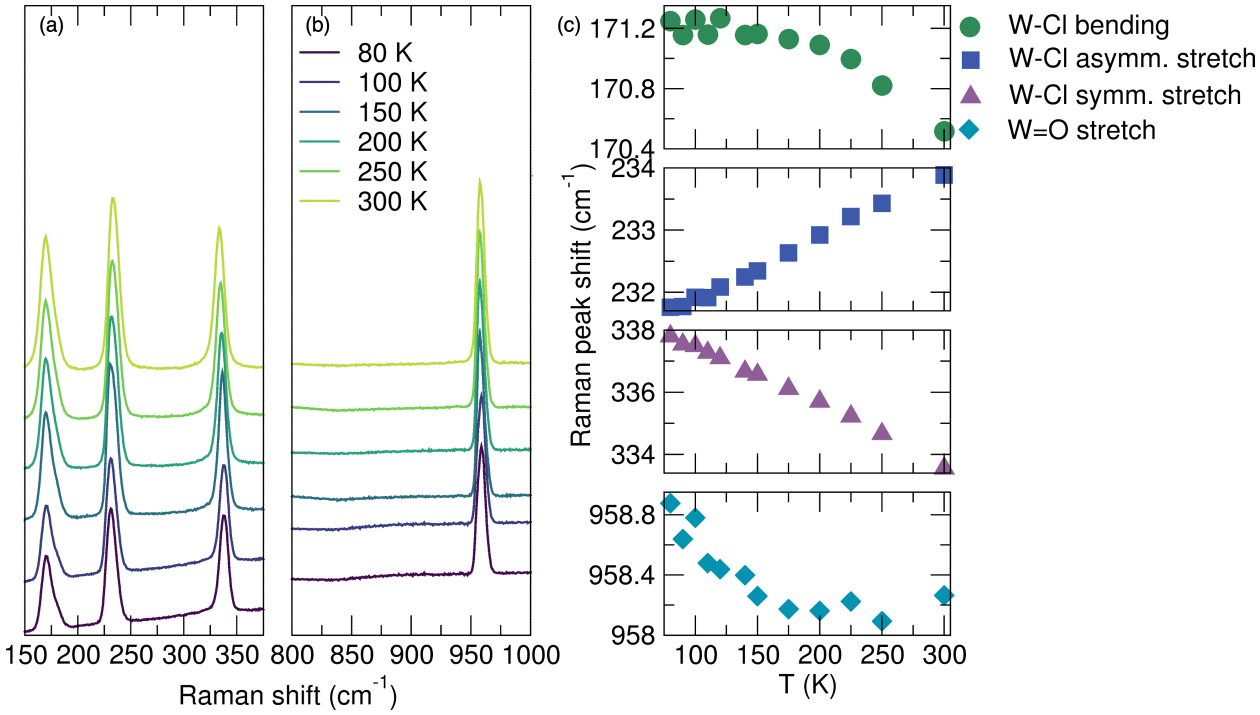

Figure 7: (a) Low frequency and (b) high frequency regions of the variable temperature Raman spectra for **6** $Cs_2WO_{1.3}Cl_{4.7}$ (c) Temperature dependence of the Raman shifts for the peaks observed in (a) and (b).

perature range. Closer analysis of the data does reveal some interesting temperature-dependent trends, as shown in Figure 7(c). First considering the lowest energy peak, which is associated with bending modes of the W–Cl bonds, the position of this peak remains relatively constant until approximately 150 K, after which it begins to decrease in energy. Next, for the peak associated with the asymmetric stretching modes, we find that this peak increases linearly in energy with temperature. In contrast, the energy of the peak for the symmetric stretch decreases linearly with temperature, which makes sense as the W–Cl bonds should increase in length with temperature. Finally, for the peak associated with the W–O stretch, the energy of this peak decreases between 80 K and 150 K, and then remains relatively constant at temperatures greater than 150 K.

The changes in the Raman trends at temperatures around 150 K correlate well with the temperature range where the changes in the emission lifetimes were observed for this compound in the 400 nm data. Given that in $Cs_2WO_{1.3}Cl_{4.7}$ the transition to the short-

lifetime process is complete at 150 K and there are changes in the trends in the W–Cl bending and W–O also around 150 K, we hypothesize that changes in vibrational modes may facilitate different emission pathways that lead to the change in lifetimes. Similarly to the other optical phenomena observed here, these changes are most likely driven by changes in the M–O bonds.

Conclusion

We have shown that compounds with the formula $Cs_2MO_xX_{6-x}$ (M = Mo or W, X = Cl or Br) exhibit intriguing near-IR emission which arises from the presence of oxygen in the $[MOX_5]^{2-}$ octahedra. Contrary to some recent reports[5,9,10] these compounds are not halides of composition Cs_2MX_6 (M = Mo, W; X = Cl, Br). The true composition and structure of these materials can be established using careful diffraction, magnetic measurements, and spectroscopy. Molecular orbital theory is applied to demonstrate how near-IR emission in these compounds arises from radiative decay from the $d_{xz,yz}$ to the d_{xy} orbital following promotion of an electron from d_{xy} to either the $d_{x^2-y^2}$ or $d_{xz,yz}$ orbitals. This picture is consistent with UV-vis absorption, photoluminescence excitation, and emission measurements. Additionally, we show that the broad emission arises from vibronic coupling to the M–O stretching modes, which we confirm via temperature-dependent emission and Raman spectroscopy. Finally, time-resolved measurements show that at low temperatures, all compounds show long emission lifetimes on the order of tens of microseconds. Between 50 K and 150 K, there is a transition to shorter emission lifetimes that coincides with energetic shifts of the M–O stretching mode. These results highlight the key role of the M–O bond in the near-IR emission observed in these compounds. While the identity of the halide anion strongly influences visible light absorption, the energy and temperature dependence of the emission are determined by the metal identity, which can be used to inform the search for other near-IR emitters.

Supporting Information

All six Crystallographic Information Files (.cif files) for the six compounds are provided. Seperately, in the Supporting Information document, powder X-ray diffraction patterns, high-resolution X-ray photoelectron spectra in relevant energy regions, and emission lifetime data are presented.

Acknowledgments

This work was supported by the U.S. Department of Energy, Office of Science, Basic Energy Sciences under award number DE-SC0024422. Experimental studies reported here made use of the shared facilities of the Materials Research Science and Engineering Center (MRSEC) at UC Santa Barbara (NSF DMR–2308708) and the the Quantum Structures Facility within the California NanoSystems Institute, supported by the University of California, Santa Barbara and the University of California, Office of the President. Time-resolved spectroscopy instrumentation at UC Santa Barbara was supported by DoD ARO DURIP award 66886LSRIP. Work performed at the Center for Nanoscale Materials, a U.S. Department of Energy Office of Science User Facility, was supported by the U.S. DOE, Office of Basic Energy Sciences, under Contract No. DE-AC02-06CH11357. E.E.M. acknowledges the NSF Graduate Research Fellowship Program under award number 2139319 and A.Z. gratefully acknowledges the Elings Postdoctoral Fellowship Program. A.K.C. thanks the Ras Al Khaimah Center for Advanced Materials for financial support. S.P. acknowledges support from the National Science Foundation Graduate Research Fellowship Program under DGE-1842165 and R.D.S. acknowledges the National Science Foundation MSN CHE-1808590.

References

(1) Wolf, N. R.; Connor, B. A.; Slavney, A. H.; Karunadasa, H. I. Doubling the Stakes: The Promise of Halide Double Perovskites. *Angew. Chem. Int. Ed.* **2021**, *60*, 16264–16278.

(2) Maughan, A. E.; Ganose, A. M.; Scanlon, D. O.; Neilson, J. R. Perspectives and Design Principles of Vacancy-Ordered Double Perovskite Halide Semiconductors. *Chem. Mater.* **2019**, *31*, 1184–1195.

(3) Gamelin, D. R.; Güdel, H. U. Spectroscopy and Dynamics of Re^{4+} Near-IR-to-Visible Luminescence Upconversion. *Inorg. Chem.* **1999**, *38*, 5154–5164.

(4) Sun, J.; Zheng, W.; Huang, P.; Zhang, M.; Zhang, W.; Deng, Z.; Yu, S.; Jin, M.; Chen, X. Efficient Near-Infrared Luminescence in Lanthanide-Doped Vacancy-Ordered Double Perovskite Cs_2ZrCl_6 Phosphors via Te^{4+} Sensitization. *Angew. Chem. Int. Ed.* **2022**, *61*, e202201993.

(5) Li, Z.; Xu, M.; Liu, W.; Wang, X.; Li, Y.; Zhou, X.; Fang, Z.; Ning, L. Broadband Near-Infrared Luminescence from Mo^{4+} in Zero-Dimensional Perovskite $Cs_2Zr(Cl,Br)_6$ with an Exceptionally High Quantum Efficiency and Thermal Stability. *Chem. Mater.* **2024**, *36*, 901–910.

(6) Tan, Z.; Li, J.; Zhang, C.; Li, Z.; Hu, Q.; Xiao, Z.; Kamiya, T.; Hosono, H.; Niu, G.; Lifshitz, E.; Cheng, Y.; Tang, J. Highly Efficient Blue-Emitting Bi-Doped Cs_2SnCl_6 Perovskite Variant: Photoluminescence Induced by Impurity Doping. *Adv. Funct. Mater.* **2018**, *28*, 1801131.

(7) Zhang, W.; Zheng, W.; Li, L.; Huang, P.; Gong, Z.; Zhou, Z.; Sun, J.; Yu, Y.; Chen, X. Dual-Band-Tunable White-Light Emission from Bi^{3+}/Te^{4+} Emitters in Perovskite-Derivative Cs_2SnCl_6 Microcrystals. *Angew. Chem. Int. Ed.* **2022**, *61*, e202116085.

(8) Wei, Y.; Dang, P.; Dai, Z.; Li, G.; Lin, J. Advances in Near-Infrared Luminescent Materials Without Cr^{3+}: Crystal Structure Design, Luminescence Properties, and Applications. *Chem. Mater.* **2021**, *33*, 5496–5526.

(9) Liu, Z.; Qin, X.; Chen, Q.; Chen, Q.; Jing, Y.; Zhou, Z.; Zhao, Y. S.; Chen, J.; Liu, X. Highly Stable Lead-Free Perovskite Single Crystals with NIR Emission Beyond 1100 nm. *Adv. Opt. Mater.* **2022**, *10*, 2201254.

(10) Mondal, B.; Shinde, A.; Rajput, P. K.; Arfin, H.; Tanwar, R.; Ghosh, P.; Nag, A. Vibronically Coupled Near-Infrared Emission and Excitation from d-d Transitions of Cs_2MX_6 (M = Mo/W, X = Cl/Br). *ACS Energy Lett.* **2024**, *9*, 819–828.

(11) Kumar, S.; Lamba, R. S.; Monga, S.; Jha, V.; Rachna; Saha, S.; Bhattacharya, S.; Sapra, S. Broad Dual Emission from $Cs_2Zr_{1-x}Mo_xCl_6$: Enhancing the NIR Emission in Lead-free Vacancy Ordered Double Perovskites. *Chem. Mater.* **2024**, *36*, 4561–4570.

(12) Morgan, E. E.; Kent, G. T.; Zohar, A.; O'Dea, A.; Wu, G.; Cheetham, A. K.; Seshadri, R. Hybrid and Inorganic Vacancy-Ordered Double Perovskites A_2WCl_6. *Chem. Mater.* **2023**, *35*, 7032–7038.

(13) Vincent, R. C.; Cheetham, A. K.; Seshadri, R. Structure and Lithium Insertion in Oxides of Molybdenum. *APL Materials* **2023**, *11*, 010902.

(14) Fergusson, J. E.; Greenaway, A. M.; Penfold, B. R. Preparative and Structural Studies of Pentahalogeno-Oxometallate(V) Salts of the Transition Metals Cr, Mo, W, Tc, Re. *Inorg. Chim. Acta* **1983**, *71*, 29–34.

(15) Greenaway, A. M. Vibrational Studies of $(MLX_5)^{n-}$ Type Compounds. Dissertation, University of Canterbury, Christchurch, New Zealand, 1976.

(16) Gray, H. B.; Hare, C. R. The Electronic Structures and Spectra of Chromyl and Molybdenyl Ions. *Inorg. Chem.* **1962**, *1*, 363–368.

(17) Hare, C. R.; Bernal, I.; Gray, H. B. The Electronic Structures and Magnetic Properties of the Chromyl and Molybdenyl Ions. *Inorg. Chem.* **1962**, *1*, 831–835.

(18) Coelho, A. A. TOPAS and TOPAS-Academic: An Optimization Program Integrating Computer Algebra and Crystallographic Objects Written in C++. *J. Appl. Crystallogr.* **2018**, *51*, 210–218.

(19) Momma, K.; Izumi, F. VESTA 3 for Three-Dimensional Visualization of Crystal, Volumetric and Morphology Data. *J. Appl. Crystallogr.* **2011**, *44*, 1272–1276.

(20) Kubelka, P. Ein Beitrag zur Optik der Farbanstriche. *Z. Phys.* **1931**, *12*, 593–601.

(21) Wojdyr, M. Fityk: A General-Purpose Peak Fitting Program. *J. Appl. Cryst.* **2010**, *43*, 1126–1128.

(22) Moulder, J. F.; Stickle, W. F.; Sobol, P. E.; Bomben, K. D. In *Handbook of X-ray Photoelectron Spectroscopy*; Chastain, J., Ed.; Perkin-Elmer Corporation: Eden Prarie, Minnesota, 1992.

(23) Mozur, E. M.; Seshadri, R. Methods and Protocols: Practical Magnetic Measurement. *Chem. Mater.* **2023**, *35*, 3450–3463.

(24) Folgueras, M. C.; Jin, J.; Gao, M.; Quan, L. N.; Steele, J. A.; Srivastava, S.; Ross, M. B.; Zhang, R.; Seeler, F.; Schierle-Arndt, K.; Asta, M.; Yang, P. Lattice Dynamics and Optoelectronic Properties of Vacancy-Ordered Double Perovskite Cs_2TeX_6 (X = Cl^-, Br^-, I^-) Single Crystals. *J. Phys. Chem. C* **2021**, *125*, 25126–25139.

(25) Griffith, W. P. Oxy-complexes and their Vibrational Spectra. *J. Chem. Soc. A* **1969**, 211–218.

(26) de Jong, M.; Seijo, L.; Meijerink, A.; Rabouw, F. T. Resolving the Ambiguity in the Relation between Stokes Shift and Huang–Rhys Parameter. *Phys. Chem. Chem. Phys.* **2015**, *17*, 16959–16969.

(27) Dar, M. I.; Jacopin, G.; Meloni, S.; Mattoni, A.; Arora, N.; Boziki, A.; Zakeeruddin, S. M.; Rothlisberger, U.; Grätzel, M. Origin of Unusual Bandgap Shift and Dual Emission in Organic-Inorganic Lead Halide Perovskites. *Sci. Adv.* **2016**, *2*, e1601156.

(28) Fabini, D. H.; Stoumpos, C. C.; Laurita, G.; Kaltzoglou, A.; Kontos, A. G.; Falaras, P.; Kanatzidis, M. G.; Seshadri, R. Reentrant Structural and Optical Properties and Large Positive Thermal Expansion in Perovskite Formamidinium Lead Iodide. *Angew. Chemie* **2016**, *128*, 15618–15622.

TOC Graphic

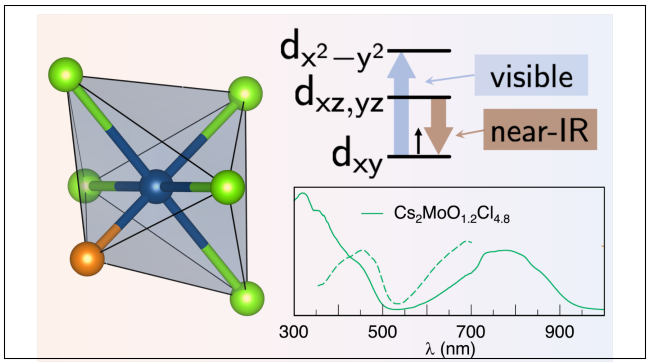
$d_{x^2-y^2}$
$d_{xz,yz}$
d_{xy}
visible
near-IR
$Cs_2MoO_{1.2}Cl_{4.8}$
300
500
700
900
λ (nm)

Supporting information for

Molecular Origins of Near-Infrared Luminescence in Molybdenum and Tungsten Oxyhalide Perovskites

Emily E. Morgan,[1] Alexandra Brumberg,[1] Shobhana Panuganti,[2] Greggory T. Kent,[1] Arava Zohar,[1] Alexander A. Mikhailovsky,[3] Mercouri G. Kanatzidis,[2] Richard D. Schaller,[2,4] Michael L. Chabinyc,[1] Anthony K. Cheetham,[1,5] and Ram Seshadri[1,3]

[1]Materials Department and Materials Research Laboratory
University of California, Santa Barbara, California 93106, United States
[2]Department of Chemistry
Northwestern University, Evanston, Illinois 60208, United States
[3]Department of Chemistry and Biochemistry
University of California, Santa Barbara, California 93106, United States
[4]Center for Nanoscale Materials
Argonne National Laboratory, Lemont, Illinois 60439, United States
[5]Department of Materials Science and Engineering
National University of Singapore, Singapore 117575, Singapore

Table of contents

Section S1. Powder X-ray diffraction

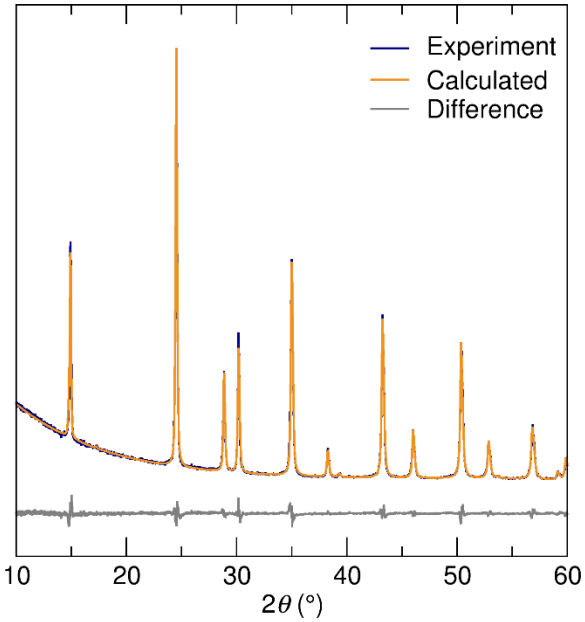

Figure S1. Powder X-ray diffraction pattern and Pawley refinement for **1** $Cs_2WO_{1.3}Cl_{4.7}$ with a calculated lattice parameter of 10.232 Å.

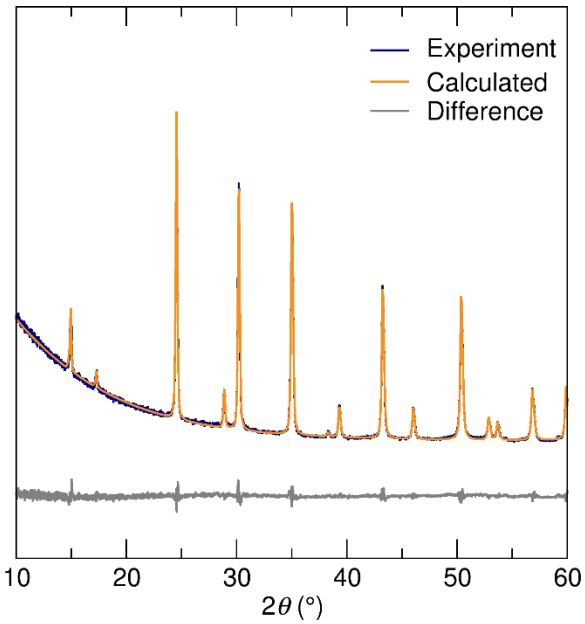

Figure S2. Powder X-ray diffraction pattern and Pawley refinement for **3** $Cs_2MoO_{1.2}Cl_{4.8}$ with a calculated lattice parameter of 10.235 Å.

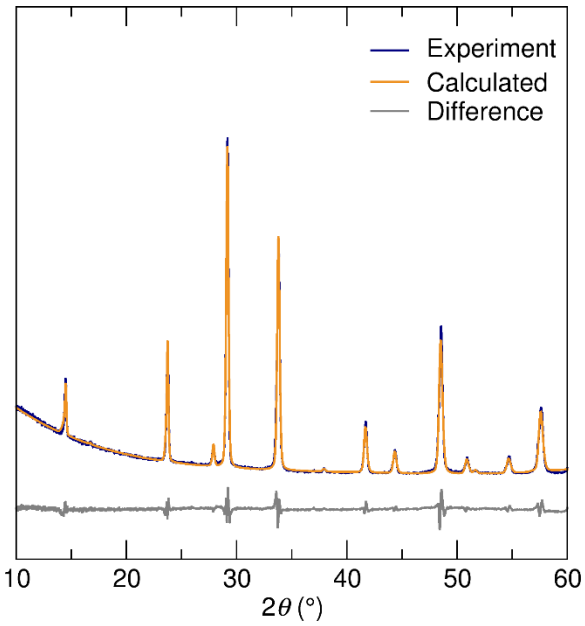

Figure S3. Powder X-ray diffraction pattern and Pawley refinement for **6** $Cs_2MoO_{1.60}Br_{4.40}$ with a calculated lattice parameter of 10.624 Å.

Section S2. XPS spectra

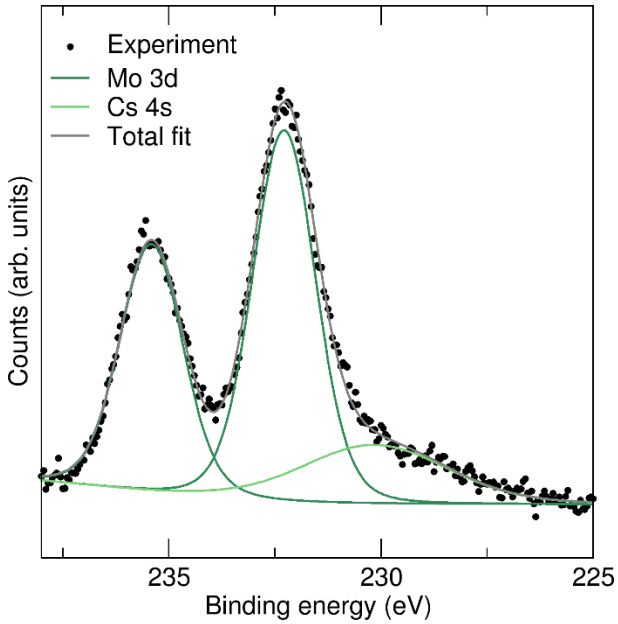

Figure S4. Molybdenum 3d high-resolution region of the XPS spectrum for $Cs_2MoO_{1.2}Cl_{4.8}$.

Table S1. Peak energies for the XPS spectrum for **1** $Cs_2MoO_{1.2}Cl_{4.8}$.

Peak assignment	Energy (eV)
Mo 3d 3/2	235.4
Mo 3d 5/2	232.3
Cs 4s	230.1

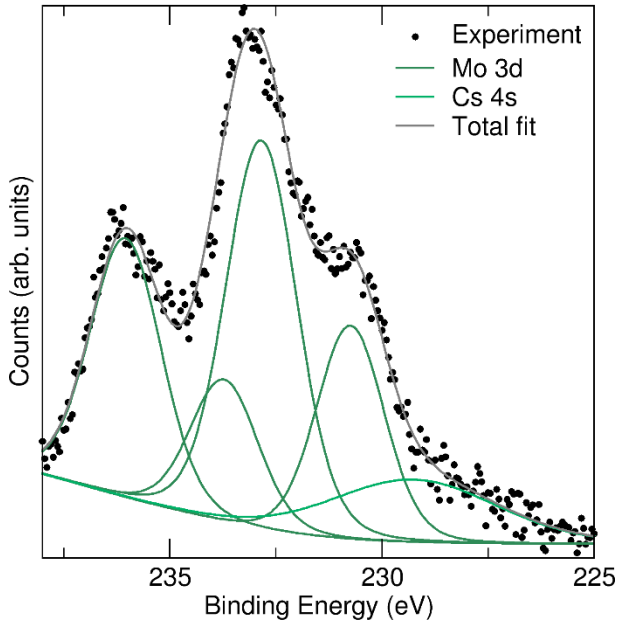

Figure S5. Molybdenum 3d high-resolution region of the XPS spectrum for **3** $Cs_2MoO_{1.60}Br_{4.40}$.

Table S2. Peak energies for the XPS spectrum for $Cs_2MoO_{1.60}Br_{4.40}$.

Peak assignment	Energy (eV)
Mo 3d 3/2 (1)	236.0
Mo 3d 5/2 (1)	232.8
Mo 3d 3/2 (2)	233.7
Mo 3d 5/2 (2)	230.7
Cs 4s	229.3

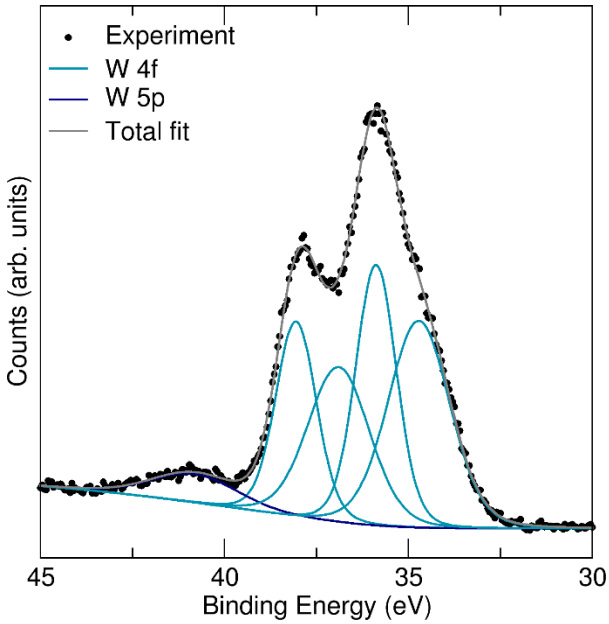

Figure S6. Tungsten *4f* high-resolution region of the XPS spectrum for **6** $Cs_2WO_{1.3}Cl_{4.7}$.

Table S3. Peak energies for the XPS spectrum for $Cs_2WO_{1.3}Cl_{4.7}$.

Peak assignment	Energy (eV)
W 4f 5/2 (1)	38.1
W 4f 7/2 (1)	35.9
W 4f 5/2 (2)	36.9
W 4f 7/2 (2)	34.7
W 5p	40.8

Section S3. Emission lifetimes

Table S4. Emission lifetimes as a function of temperature for **1** $Cs_2MoO_{1.2}Cl_{4.8}$ excited at 800 nm.

	A_1	τ_1 (µs)	A_2	τ_2 (µs)
77 K	86 %	7.0	14 %	25.2
100 K	87 %	6.7	13 %	24.6
125 K	87 %	6.5	13 %	23.9
150 K	87 %	6.1	13 %	22.6
175 K	88 %	5.9	12 %	21.6
200 K	87 %	5.4	13 %	19.9
250 K	88 %	5.4	12 %	19.1
300 K	88 %	4.8	12 %	16.6

Table S5. Emission lifetimes as a function of temperature for **1** $Cs_2MoO_{1.2}Cl_{4.8}$ excited at 400 nm.

	A_1	τ_1 (µs)	A_2	τ_2 (µs)
2.7 K	100 %	95.6		
3 K	100 %	96.6		
5 K	100 %	94.5		
10 K	100 %	94.9		
25 K	100 %	95.2		
50 K	100 %	82.7		
75 K	51 %	65.3	49 %	25.6
100 K	29 %	49.7	71 %	15.3
150 K	20 %	30.7	80 %	7.5
200 K	16 %	24.1	84 %	5.5
250 K	13 %	20.5	87 %	4.4
300 K	13 %	16.3	87 %	3.7
330 K	12 %	15.4	88 %	3.4
350 K	10 %	18.3	90 %	3.5

Table S6. Emission lifetimes as a function of temperature for **3** $Cs_2MoO_{1.60}Br_{4.40}$ excited at 800 nm.

	A_1	τ_1 (µs)	A_2	τ_2 (µs)
77 K	89 %	2.2	11 %	9.4
100 K	90 %	1.9	10 %	7.8
125 K	90 %	1.5	10 %	6.5
150 K	91 %	1.3	9 %	5.4
175 K	91 %	1.1	9 %	4.6
200 K	91 %	0.9	9 %	3.9
250 K	92 %	0.8	8 %	3.3
300 K	91 %	0.7	9 %	3.0

Table S7. Emission lifetimes as a function of temperature for **3** $Cs_2MoO_{1.60}Br_{4.40}$ excited at 400 nm.

	A_1	τ_1 (µs)	A_2	τ_2 (µs)
2.7 K	100 %	81.9		
3 K	100 %	81.1		
5 K	100 %	81.8		
10 K	100 %	80.3		
25 K	100 %	80.4		
50 K	100 %	67.9		
75 K	32 %	65.6	68 %	18.5
100 K	20 %	43.4	80 %	8.6
150 K	8 %	36.6	92 %	5.1
200 K	5 %	27.5	95 %	3.1
250 K	3 %	22.9	97 %	2.1
300 K	4 %	13.7	96 %	1.9
330 K	4 %	12.5	96 %	1.9
350 K	4 %	16.0	96 %	2.0

Table S8. Emission lifetimes as a function of temperature for **6** $Cs_2WO_{1.3}Cl_{4.7}$ excited at 800 nm.

	A_1	τ_1 (µs)	A_2	τ_2 (µs)
77 K	58 %	13.4	42 %	33.5
100 K	74 %	9.3	26 %	25.0
125 K	77 %	6.1	23 %	17.8
150 K	79 %	4.6	21 %	13.5
175 K	79 %	3.6	21 %	10.9
200 K	77 %	2.9	23 %	8.9
250 K	81 %	2.5	19 %	7.3
300 K	88 %	2.2	12 %	6.4

Table S9. Emission lifetimes as a function of temperature for **6** $Cs_2WO_{1.3}Cl_{4.7}$ excited at 400 nm.

	A_1	τ_1 (µs)	A_2	τ_2 (µs)
2.7 K	100 %	45.9		
3 K	100 %	45.8		
5 K	100 %	46.1		
10 K	100 %	46.1		
25 K	100 %	47.5		
50 K	100 %	40.2		
75 K	36 %	37.3	64 %	12.2
100 K	17 %	32.0	83 %	8.1
150 K			100 %	7.2
200 K			100 %	5.0
250 K			100 %	3.8
300 K			100 %	3.0
330 K			100 %	3.0
350 K			100 %	2.8